Heterogeneously integrated III–V/silicon dual-mode distributed feedback laser array for terahertz generation

Haifeng Shao,[1,2,*] Shahram Keyvaninia,[1] Mathias Vanwolleghem,[3] Guillaume Ducournau,[3] Xiaoqing Jiang,[2] Geert Morthier,[1] Jean-Francois Lampin,[3] and Gunther Roelkens[1]

[1]*Photonics Research Group, INTEC Department, Ghent University-IMEC, Sint-Pietersnieuwstraat 41, B-9000 Ghent, Belgium*

[2]*Department of Information Science and Electronic Engineering, Zhejiang University, Hang Zhou 310027, China*

[3]*Terahertz Photonics group, IEMN, CNRS 8520, Universite Lille 1, 59652 Villeneuve d'Ascq Cedex, France*

**Corresponding author: hshao@intec.ugent.be*

Received July 8, 2014; revised October 13, 2014; accepted October 15, 2014; posted October 16, 2014 (Doc. ID 216511); published November 5, 2014

We demonstrate an integrated distributed feedback (DFB) laser array as a dual-wavelength source for narrowband terahertz (THz) generation. The laser array is composed of four heterogeneously integrated III–V-on-silicon DFB lasers with different lengths enabling dual-mode lasing tolerant to process variations, bias fluctuations, and ambient temperature variations. By optical heterodyning the two modes emitted by the dual-wavelength DFB laser in the laser array using a THz photomixer composed of an uni-traveling carrier photodiode (UTC-PD), a narrow and stable carrier signal with a frequency of 0.357 THz is generated. The central operating frequency and the emitted terahertz wave linewidth are analyzed, along with their dependency on the bias current applied to the laser diode and ambient temperature. © 2014 Optical Society of America

OCIS codes: (140.3490) Lasers, distributed-feedback; (250.5300) Photonic integrated circuits; (060.5625) Radio frequency photonics.

http://dx.doi.org/10.1364/OL.39.006403

Among future applications of sub-millimeter waves, THz wireless communication is considered as an excellent candidate to meet the rapidly increasing demand for broadband wireless networking, due to its inherently higher bandwidth compared to microwave solutions [1,2]. In terms of continuous wave (CW) THz carrier signal-generation techniques, optical heterodyning of two wavelengths in an uni-traveling carrier photodiode (UTC-PD) is one of the most promising approaches [3]. For communications applications, the spectral purity of the carrier signal is a key point. Indeed, in the photomixing case, the characteristics of the THz signal heavily rely on the spectral purity and frequency stability of the used lasers. Moreover, in order to realize a compact THz wireless transmitter operating at high bit rates, high-speed optical modulators and a UTC-PD also need to be integrated in the transmitter. To tackle this challenge, photonic integration allows integrating such devices on a single chip, improving the cost and compactness. Silicon photonics is an attractive platform for such integration given the high-volume manufacturing capability. In this Letter, we demonstrate a dual-wavelength laser integrated on a silicon photonics platform. The combination of two discrete free-running lasers as an optical beat source has been demonstrated for THz generation [4], but this approach suffers from limited spectral purity of the beat note and is prone to long-term drift of its frequency. On the contrary, monolithically integrated dual-wavelength lasers, which are compact, cost-effective and experience similar environmental fluctuations leading to a reduction of the drift of the THz signal, have been shown to be efficient solutions. Recently several structures including spectrum tailored semiconductor Fabry–Perot (FP) lasers [5], multisection distributed feedback (DFB) lasers [6,7], two independent lasers on a chip with optical combiners [8–10] and dual-wavelength single-cavity lasers [11,12] have been demonstrated. The spectrum of the FP is tailored through local etching of the guide leading to a poor side-mode-suppression ratio (SMSR). The generated THz signal is not really clean with a lot of mode hops [5]. The multisection structure with one phase [6] or distributed Bragg reflector (DBR) section [7] between two DFB lasers have shown great potential for tunability. However, the need for multiple injection currents makes the control more difficult, which can again result in instability of the generated THz signal. Although a multi-wavelength laser with an arrayed waveguide grating (AWG) as an intracavity filter has achieved a narrow linewidth of 130 kHz [8,9], this structure is quite complex. Moreover its operation was limited to a beat note not exceeding 90 GHz, therefore limiting the potential data rate. The device would be greatly simplified if the two wavelengths are generated simultaneously in a simple single cavity structure [13]. In this report, we report a single-cavity-based dual-mode III–V/silicon DFB laser using which a stable and narrowband THz signal at 0.357 THz is generated through optical heterodyning in a UTC-PD. The THz signal shows a good tolerance to temperature and injection current variations. It is worth noting that the dual-mode laser is one device from a four-channel laser array that is designed to be able to generate a THz signal taking into account processing variations, bias current variations, and temperature fluctuations. The integration on a silicon platform paves the way toward a fully integrated on-chip THz transmitter.

The DFB laser array is fabricated by heterogeneously integrating a III–V layer onto the silicon waveguide circuit containing the distributed feedback gratings through adhesive wafer bonding technology. The heterogeneous integration technology is described in detail in [14]. The 3D layout of the laser cavity and a longitudinal

 © 2014 Optical Society of America

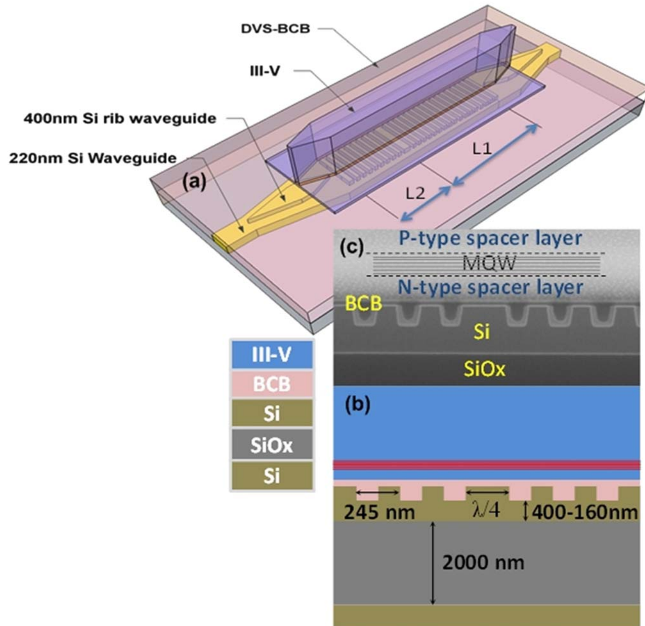

Fig. 1. III–V/Si DFB dual-mode laser design. (a) Three-dimensional view of the III–V/Si DFB dual-mode laser. (b) Schematic longitudinal cross-section of the laser structure. (c) SEM picture of the actual device.

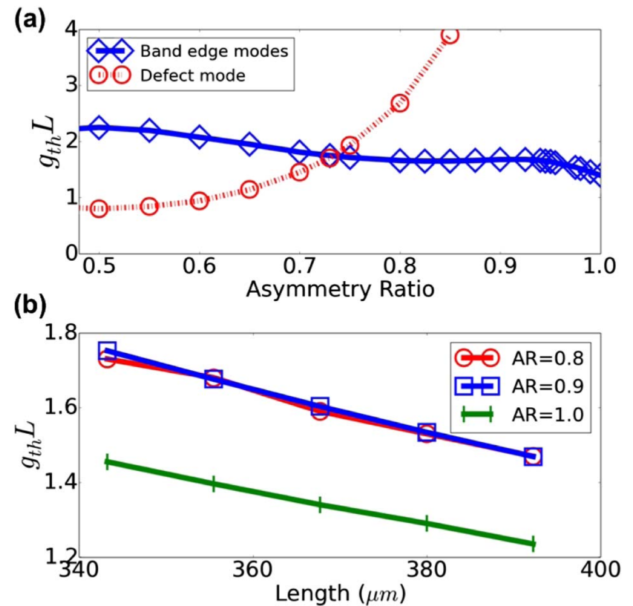

Fig. 2. Normalized threshold gain $g_{\mathrm{th}}L$ (a) versus asymmetry ratio (AR); (b) as a function of DFB length for various values of AR.

cross-section of the laser geometry are depicted in Fig. 1. The laser mode is predominantly confined in the active III–V waveguide, while the evanescent tail feels the silicon grating underneath. Optical coupling from the III–V waveguide layer to the silicon waveguide layer is realized using a III–V/silicon spot-size converter structure. The structure is described in more detail in [15]. In this work, two variables are assessed in order to reach dual-mode operation: the laser cavity length and the position of the $\lambda/4$ phase shift. Using a $\lambda/4$ phase shift located in the middle of the device, the DFB laser will exhibit single-mode lasing operation at the Bragg wavelength. However in our case, the $\lambda/4$ phase shifter is placed strongly asymmetric in the first-order gratings. The asymmetry ratio (AR) is defined as $L_1/(L_1 + L_2)$ in which $L_1 + L_2$ is the total DFB length L.

The normalized threshold gain ($g_{\mathrm{th}}L$) for the two band-edge modes positioned symmetrically on either side of the grating stop band and that of the defect mode located in the middle of the stop band versus AR and L are calculated according to the method in [16], as shown in Fig. 2. In the simulation, a DFB structure with two non-reflecting ends is assumed and a coupling strength of 76.9 cm^{-1} is used, as was extracted from the experimental results, which will be described later. From Fig. 2(a) one can see that in the symmetric device (AR = 0.5), the defect mode has the lowest threshold, as expected. The situation changes however when the asymmetry becomes larger, in which case the two band edge modes have the lowest threshold with the limiting case of a defect-free DFB laser (AR = 1). A plateau in the normalized threshold gain can be observed for AR ranging from 0.81 to 0.93. Figure 2(b) shows $g_{\mathrm{th}}L$ as a function of L for three different values of AR. While both band edge modes have the same threshold gain, this does not necessarily mean that the laser will work in dual-mode regime. For that to occur, both wavelengths should also experience the same gain, i.e., both modes should lie symmetrically around the material gain peak wavelength. This gain peak wavelength, however, shifts to shorter wavelengths with higher carrier injection. This gives us a degree of freedom to achieve dual-mode lasing: by changing the threshold gain of the band edge modes (using L and AR), dual-mode operation can be obtained by exactly placing the gain peak in between the two modes. Since the exact position of the gain peak is difficult to control during III–V layer growth, a set of lasers are to be integrated with different L and AR, such that one of them shows dual-wavelength operation under particular conditions of temperature and bias current. In our experiment, a 4-channel DFB array was fabricated in which the laser length varied between 392 and 343 μm, while the asymmetry ratio was chosen in the region of the plateau (AR between 0.81 and 0.93) in Fig. 2.

The optical spectra of these four devices at an injection current of 100 and 140 mA, respectively, are shown in Figs. 3(a)–3(d). The temperature during this experiment was fixed at 15°C. The longest device lases at the longer wavelength band-edge mode, while the shortest device lases at the short-wavelength band-edge mode. This is due to the shift of the gain peak toward shorter wavelengths as the threshold gain increases when the cavity length is reduced. At 100 mA, current DFB No. 3 shows dual-mode behavior, with a wavelength spacing of 2.78 nm (corresponding to a grating coupling strength of 76.9 cm^{-1}). At 140 mA, the power imbalance between both modes increases again due to a red-shift in the gain peak due to self-heating of the device. The temperature of the laser can also be used as a parameter to obtain dual-wavelength behavior. This is illustrated in Fig. 3(e) showing dual mode behavior of DFB No. 4 at 29.5°C and 140 mA, with a spacing of 2.74 nm.

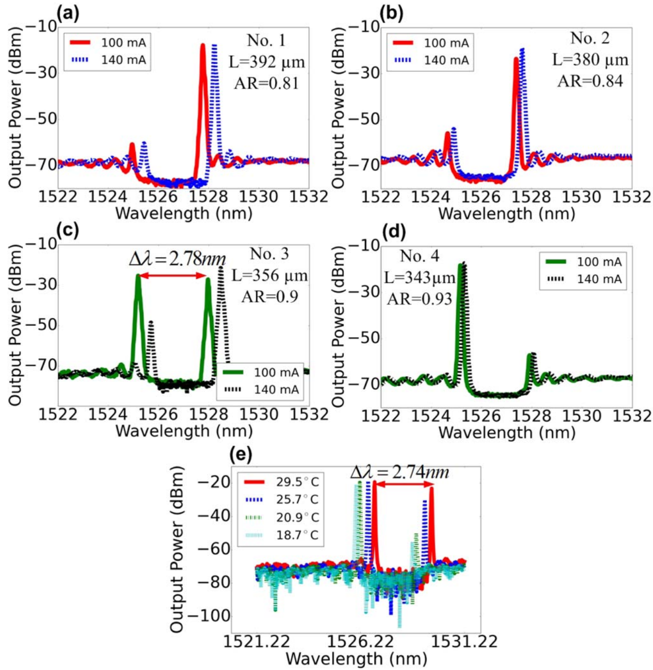

Fig. 3. Optical spectra from the DFB laser array at 100 and 140 mA with different lengths L and asymmetry ratio R. (a) No. 1: $L = 392$ μm, AR = 0.81. (b) No. 2: $L = 380$ μm, AR = 0.84 (c) No. 3: $L = 356$ μm, AR = 0.90. (d) No. 4: $L = 343$ μm, AR = 0.93. (e) Optical spectrum variation of device No. 4 with temperature at 140 mA. The lower noise floor in between the laser lines is related to the stop band induced by the DFB grating, which prevents the outcoupling of spontaneous emission within this wavelength range.

The experimental setup for THz generation is presented in Fig. 4 and consists of two key components: the III–V/silicon dual-mode DFB laser (device No. 3) from the laser array denoted as device under test (DUT) and an optimized UTC-PD with a monolithically integrated transverse-electromagnetic-horn-antenna (TEM-HA) [17] for photomixing at THz frequencies. The DUT has a threshold current of 36 mA at 15°C. As shown in Fig. 3(c), at 100 mA bias current, the two longitudinal modes are positioned at 1525.19 and 1527.97 nm, respectively, with a wavelength spacing of 2.78 nm. More than 40 dB dual-mode-to-noise suppression ratio is obtained. The DUT emission is collected in a standard single-mode fiber via fiber-to-chip grating-coupler structures in the SOI photonic circuit. The fiber-coupled output power is −10 dBm at 100 mA drive current. A fiber isolator prevents reflections back into the laser cavity. The optical signal is amplified by an erbium-doped fiber amplifier (EDFA) up to 21.5 dBm, corresponding to a photocurrent in the UTC-PD of 1.3 mA. A polarization controller (PC) is used to adjust the polarization state before the UTC-PD. An optical spectrum analyzer (OSA) allows parallel monitoring of the optical spectrum. The THz radiation emitted from the TEM-HA is collected and focused by a system of polymer lenses onto the horn of a WR 2.8 sub-harmonic mixer (260–400 GHz, MIX) [5]. This mixer is driven by a 7.5–15-GHz local oscillator (LO) followed by an active multiplier. The intermediate frequency signal centered at 404.4 MHz is analyzed using a Rhode & Schwarz FSU 67-GHz electrical spectrum analyzer (ESA).

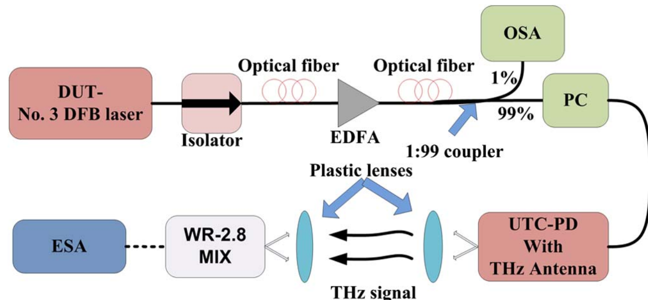

Fig. 4. Experimental setup for the generation and characterization of the THz signal. Optical fiber is represented with a solid line, and the electrical path is represented by a dashed line.

A typical obtained THz spectrum with a resolution bandwidth (RBW) of 1 MHz is shown in Fig. 5(a). The Lorentzian fit shows a −3 dB linewidth of 4.2 MHz. Taking into account the down-conversion losses of the mixer, the THz received power is about −30 dBm. This value approaches the required power levels for operational indoor point-to-point wireless THz communications systems handling multi-Gbit/s data rates [18]. The electrical signal-to-noise ratio (SNR) is about 40 dB. The long-term frequency drift is also reasonable, showing a peak-to-peak frequency jitter of about 28 MHz during 30 s as illustrated in Fig. 5(b). No substantial THz power fluctuations were observed over the measurement time (30 s) indicating that stable dual mode lasing is obtained. The frequency drift is attributed to drift of the injection current in the device given the relatively large dependence of the THz emission frequency on the injection current, as discussed below. The robustness of the DUT to bias current and temperature variation was assessed. Figure 6(a) shows the THz power for a range of bias

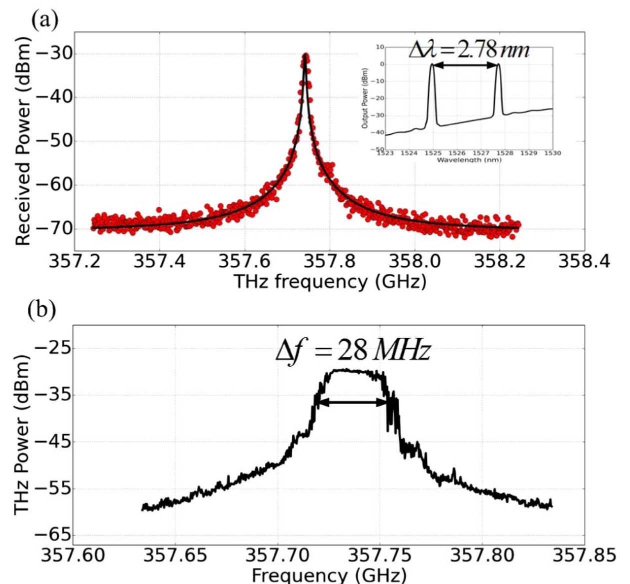

Fig. 5. (a) The 357.7-GHz electrical beat note obtained from the UTC-PD at 85 mA and 15°C (in red) with Lorentzian fit (black). The inset is the corresponding optical spectrum for the same bias and temperature condition. (b) Central frequency jitter with a long sweep time of 30 s. Resolution bandwidth RBW = 1 MHz, video bandwidth VBW = 3 MHz.

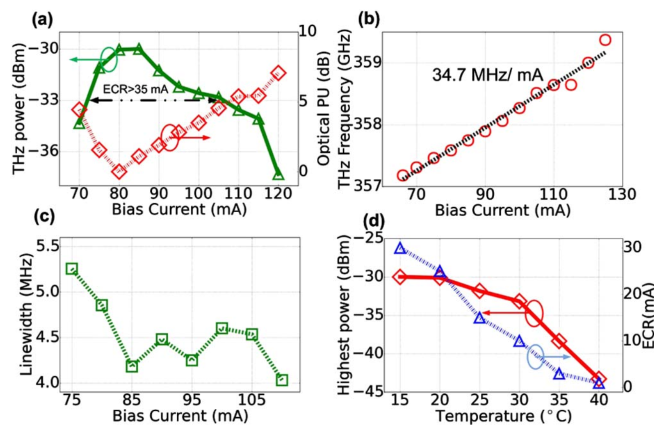

Fig. 6. Variation of the THz signal as a function of bias current at 15°C: (a) generated THz power and optical power unbalance (PU); (b) THz frequency; (c) linewidth. (d) THz power and effective current range as a function of temperature.

currents between 70 and 120 mA for device No. 3 at 15°C. The effective current range (ECR) in which the THz power decreases 3 dB from its maximum is 32 mA (73–105 mA) which is quite broad due to the limited change of optical power unbalance (PU) between the two modes of the DUT as a function of bias current as shown in Fig. 6(a). The THz central frequency increases linearly with bias current with a slope of 34.7 MHz/mA as shown in Fig. 6(b). The linewidth of the THz signal as a function of the bias current is plotted in Fig. 6(c). The linewidth does not change much and fluctuates around 4.5 MHz. Furthermore, the influence of the temperature on the behavior of the THz signal is also investigated in Fig. 6(d). As the temperature increases, the effective current range shrinks and the generated THz power decreases. Device No. 3 shows reasonable performance up to 30°C with an effective range of bias currents of at least 10 mA at 30°C. However, as discussed above, at higher temperatures DFB No. 4 will start to emit dual mode. Thereby, this approach of integrating a laser array can show good tolerance against bias current and temperature variations.

In conclusion, we have demonstrated a III–V on silicon laser structure allowing THz signal generation by optical heterodyning two modes simultaneously lasing in a single DFB laser cavity. This dual-mode laser is part of a laser array that is constructed by sweeping the device length and position of the quarter-wave phase shift. Simulation results show that the device length is the dominant factor for changing the threshold gain and therefore moving the gain peak. The gradual gain peak shift guarantees that at least one device from the laser array has stable dual-mode operation. The generated THz signal has a linewidth of 4.2 MHz and a frequency of 0.357 THz, featuring good robustness against bias current and temperature instabilities. This result is the first step toward an on-chip robust and compact THz emitter fully integrated on silicon.

Haifeng Shao acknowledges the support of the China Scholarship Council.

References

1. J. Federici and L. Moeller, J. Appl. Phys. **107**, 111101 (2010).
2. S. Koenig, D. Lopez-Diaz, J. Antes, F. Boes, R. Henneberger, A. Leuther, A. Tessmann, R. Schmogrow, D. Hillerkuss, R. Palmer, T. Zwick, C. Koos, W. Freude, O. Ambacher, J. Leuthold, and I. Kallfass, Nat. Photonics **7**, 977 (2013).
3. D. Saeedkia and S. Safavi-Naeini, J. Lightwave Technol. **26**, 2409 (2008).
4. B. Sartorius, M. Schlak, D. Stanze, H. Roehle, H. Kunzel, D. Schmidt, H. G. Bach, R. Kunkel, and M. Schell, Opt. Express **17**, 15001 (2009).
5. S. Latkowski, J. P. Cetina, R. M. Basilio, P. Landais, G. Ducournau, A. Beck, E. Peytavit, T. Akalin, and J.-F. Lampin, Appl. Phys. Lett. **96**, 241106 (2010).
6. N. Kim, J. Shin, E. Sim, C. W. Lee, D.-S. Yee, M. Y. Jeon, Y. Jang, and K. H. Park, Opt. Express **17**, 13851 (2009).
7. Y.-H. Lo, Y.-C. Wu, S.-C. Hsu, Y.-C. Hwang, B.-C. Chen, and C.-C. Lin, Opt. Express **22**, 13125 (2014).
8. G. Carpintero, E. Rouvalis, K. Lawniczuk, M. Fice, C. C. Renaud, X. J. M. Leijtens, E. A. J. M. Bente, M. Chitoui, F. van Dijk, and A. J. Seeds, Opt. Lett. **37**, 3657 (2012).
9. G. Carpintero, K. Balakier, Z. Yang, R. C. Guzman, A. Corradi, A. Jimenez, G. Kervella, M. J. Fice, M. Lamponi, M. Chtioui, F. van Dijk, C. C. Renaud, A. Wonfor, E. A. J. M. Bente, R. V. Penty, I. H. White, and A. J. Seeds, J. Lightwave Technol. **32**, 3495 (2014).
10. N. Zhang, X. Cai, and S. Yu, Photon. Res. **2**, B11 (2014).
11. A. Klehr, J. Fricke, A. Knauer, G. Erbert, M. Walther, R. Wilk, M. Mikulics, and M. Koch, IEEE J. Sel. Top. Quantum Electron. **14**, 289 (2008).
12. N. Kim, S.-P. Han, H.-C. Ryu, H. Ko, J.-W. Park, D. Lee, M. Y. Jeon, and K. H. Park, Opt. Express **20**, 17496 (2012).
13. M. Tani, O. Morikawa, S. Matsuura, and M. Hangyo, Semicond. Sci. Technol. **20**, S151 (2005).
14. G. Roelkens, L. Liu, D. Liang, R. Jones, A. Fang, B. Koch, and J. Bowers, Laser Photon. Rev. **4**, 751 (2010).
15. S. Keyvaninia, S. Verstuyft, L. van Landschoot, F. Lelarge, G.-H. Duan, S. Messaoudene, J. M. Fedeli, T. De Vries, B. Smalbrugge, E. J. Geluk, J. Bolk, M. Smit, G. Morthier, D. van Thourhout, and G. Roelkens, Opt. Lett. **38**, 5434 (2013).
16. S. L. McCall and P. M. Platzman, IEEE J. Quantum Electron. **21**, 1899 (1985).
17. A. Beck, G. Ducournau, M. Zaknoune, E. Peytavit, T. Akalin, J.-F. Lampin, F. Mollot, F. Hindle, C. Yang, and G. Mouret, Electron. Lett. **44**, 1320 (2008).
18. G. Ducournau, P. Szriftgiser, A. Beck, D. Bacquet, F. Pavanello, E. Peytavit, M. Zaknoune, T. Akalin, and J.-F. Lampin, IEEE Trans. Terahertz Sci. Tech. **4**, 328 (2014).